

# Unambiguous demonstration of soliton evolution in slow-light silicon photonic crystal waveguides with SFG-XFROG

Xiujian Li,<sup>1,\*</sup> Jiali Liao,<sup>1</sup> Yongming Nie,<sup>2</sup> Matthew Marko,<sup>3,4</sup> Hui Jia<sup>1</sup>, Ju Liu,<sup>1</sup>  
Xiaochun Wang,<sup>1</sup> and Chee Wei Wong<sup>3,5,6</sup>

<sup>1</sup> College of Science, National University of Defense Technology, Changsha, Hunan 410073, China

<sup>2</sup> China Satellite Maritime Tracking and Controlling Department, Jiangyin, Jiangsu, 214431, China

<sup>3</sup> Optical Nanostructures Laboratory, Mechanical Engineering, Columbia University, New York, New York 10027, USA

<sup>4</sup> Navy Air Warfare Center Aircraft Division (NAWCAD), Joint Base McGuire-Dix-Lakehurst, Lakehurst NJ 08733, USA

<sup>5</sup> Mesoscopic Optics and Quantum Electronics Laboratory, Electrical Engineering, University of California, Los Angeles, CA 90095, USA

<sup>6</sup> cheewei.wong@ucla.edu

xjli@nudt.edu.cn

**Abstract:** We demonstrate the temporal and spectral evolution of picosecond soliton in the slow light silicon photonic crystal waveguides (PhCWs) by sum frequency generation cross-correlation frequency resolved optical grating (SFG-XFROG) and nonlinear Schrödinger equation (NLSE) modeling. The reference pulses for the SFG-XFROG measurements are unambiguously pre-characterized by the second harmonic generation frequency resolved optical gating (SHG-FROG) assisted with the combination of NLSE simulations and optical spectrum analyzer (OSA) measurements. Regardless of the inevitable nonlinear two photon absorption, high order soliton compressions have been observed remarkably owing to the slow light enhanced nonlinear effects in the silicon PhCWs. Both the measurements and the further numerical analyses of the pulse dynamics indicate that, the free carrier dispersion (FCD) enhanced by the slow light effects is mainly responsible for the compression, the acceleration, and the spectral blue shift of the soliton.

©2015 Optical Society of America

**OCIS codes:** (320.7110) Ultrafast nonlinear optics; (320.7130) Ultrafast processes in condensed matter, including semiconductors; (190.5530) Pulse propagation and temporal solitons.

---

## References and links

1. A. V. Velasco, P. Cheben, P. J. Bock, A. Delâge, J. H. Schmid, J. Lapointe, S. Janz, M. L. Calvo, D. X. Xu, M. Florjańczyk, and M. Vachon, "High-resolution Fourier-transform spectrometer chip with microphotonic silicon spiral waveguides," *Opt. Lett.* **38**(5), 706–708 (2013).
2. K. Liu, W. Xu, Z. H. Zhu, W. M. Ye, X. D. Yuan, and C. Zeng, "Wave propagation in deep-subwavelength mode waveguides," *Opt. Lett.* **37**(14), 2826–2828 (2012).
3. T. Baba, "Slow light in photonic crystals," *Nat. Photonics* **2**(8), 465–473 (2008).
4. Y. Hamachi, S. Kubo, and T. Baba, "Slow light with low dispersion and nonlinear enhancement in a lattice-shifted photonic crystal waveguide," *Opt. Lett.* **34**(7), 1072–1074 (2009).
5. C. Monat, B. Corcoran, M. Ebnali-Heidari, C. Grillet, B. J. Eggleton, T. P. White, L. O'Faolain, and T. F. Krauss, "Slow light enhancement of nonlinear effects in silicon engineered photonic crystal waveguides," *Opt. Express* **17**(4), 2944–2953 (2009).
6. B. Corcoran, C. Monat, C. Grillet, D. J. Moss, B. J. Eggleton, T. P. White, L. O'Faolain, and T. F. Krauss, "Green light emission in silicon through slow-light enhanced third-harmonic generation in photonic-crystal waveguides," *Nat. Photonics* **3**(4), 206–210 (2009).
7. K. Inoue, H. Oda, N. Ikeda, and K. Asakawa, "Enhanced third-order nonlinear effects in slow-light photonic-crystal slab waveguides of line-defect," *Opt. Express* **17**(9), 7206–7216 (2009).

8. D. Dai and J. E. Bowers, "Novel concept for ultracompact polarization splitter-rotator based on silicon nanowires," *Opt. Express* **19**(11), 10940–10949 (2011).
9. V. R. Almeida, C. A. Barrios, R. R. Panepucci, and M. Lipson, "All-optical control of light on a silicon chip," *Nature* **431**(7012), 1081–1084 (2004).
10. A. Blanco-Redondo, C. Husko, D. Eades, Y. Zhang, J. Li, T. F. Krauss, and B. J. Eggleton, "Observation of soliton compression in silicon photonic crystals," *Nat. Commun.* **5**, 3160 (2014).
11. D. T. H. Tan, P. C. Sun, and Y. Fainman, "Monolithic nonlinear pulse compressor on a silicon chip," *Nat. Commun.* **1**(8), 116 (2010).
12. P. Colman, C. Husko, S. Combrié, I. Sagnes, C. W. Wong, and A. De Rossi, "Temporal solitons and pulse compression in photonic crystal waveguides," *Nat. Photonics* **4**(12), 862–868 (2010).
13. J. F. McMillan, M. Yu, D. L. Kwong, and C. W. Wong, "Observation of four-wave mixing in slow-light silicon photonic crystal waveguides," *Opt. Express* **18**(15), 15484–15497 (2010).
14. C. Monat, M. Ebnali-Heidari, C. Grillet, B. Corcoran, B. J. Eggleton, T. P. White, L. O'Faolain, J. Li, and T. F. Krauss, "Four-wave mixing in slow light engineered silicon photonic crystal waveguides," *Opt. Express* **18**(22), 22915–22927 (2010).
15. D. W. Kim, S. H. Kim, S. H. Lee, H. S. Jong, J. M. Lee, H. Lee, and K. H. Kim, "Enhanced four-wave-mixing effects by large group indices of one-dimensional silicon photonic crystal waveguides," *Opt. Express* **21**(24), 30019–30029 (2013).
16. J. Li, L. O'Faolain, and T. F. Krauss, "Four-wave mixing in slow light photonic crystal waveguides with very high group index," *Opt. Express* **20**(16), 17474–17479 (2012).
17. S. Kocaman, M. S. Aras, N. C. Panoiu, M. Lu, and C. W. Wong, "On-chip optical filters with designable characteristics based on an interferometer with embedded silicon photonic structures," *Opt. Lett.* **37**(4), 665–667 (2012).
18. R. Antos, V. Vozda, and M. Veis, "Plane wave expansion method used to engineer photonic crystal sensors with high efficiency," *Opt. Express* **22**(3), 2562–2577 (2014).
19. J. Hendrickson, R. Soref, J. Sweet, and W. Buchwald, "Ultrasensitive silicon photonic-crystal nanobeam electro-optical modulator: design and simulation," *Opt. Express* **22**(3), 3271–3283 (2014).
20. B. Corcoran, M. D. Pelusi, C. Monat, J. Li, L. O'Faolain, T. F. Krauss, and B. J. Eggleton, "Ultracompact 160 Gbaud all-optical demultiplexing exploiting slow light in an engineered silicon photonic crystal waveguide," *Opt. Lett.* **36**(9), 1728–1730 (2011).
21. B. Corcoran, C. Monat, M. Pelusi, C. Grillet, T. P. White, L. O'Faolain, T. F. Krauss, B. J. Eggleton, and D. J. Moss, "Optical signal processing on a silicon chip at 640Gb/s using slow-light," *Opt. Express* **18**(8), 7770–7781 (2010).
22. Y. Xu, C. Caer, D. Gao, E. Cassan, and X. Zhang, "High efficiency asymmetric directional coupler for slow light slot photonic crystal waveguides," *Opt. Express* **22**(9), 11021–11028 (2014).
23. E. Engin, D. Bonneau, C. M. Natarajan, A. S. Clark, M. G. Tanner, R. H. Hadfield, S. N. Dorenbos, V. Zwiller, K. Ohira, N. Suzuki, H. Yoshida, N. Iizuka, M. Ezaki, J. L. O'Brien, and M. G. Thompson, "Photon pair generation in a silicon micro-ring resonator with reverse bias enhancement," *Opt. Express* **21**(23), 27826–27834 (2013).
24. T. Chen, J. Sun, and L. Li, "Modal theory of slow light enhanced third-order nonlinear effects in photonic crystal waveguides," *Opt. Express* **20**(18), 20043–20058 (2012).
25. M. D. Marko, X. Li, J. Zheng, J. Liao, M. Yu, G.-Q. Lo, D.-L. Kwong, C. A. Husko, and C. W. Wong, "Phase-resolved observations of temporal soliton pulse propagation in silicon nanowires," *Appl. Phys. Lett.* **103**, 021103 (2013).
26. N. Tsurumachi, K. Hikosaka, X.-L. Wang, M. Ogura, N. Watanabe, and T. Hattori, "Observation of ultrashort pulse propagation anisotropy in a semiconductor quantum nanostructure optical waveguide by cross-correlation frequency resolved optical gating spectroscopy," *J. Appl. Phys.* **94**(4), 2616–2621 (2003).
27. A. Efimov and A. J. Taylor, "Cross-correlation frequency-resolved optical gating for studying ultrashort-pulse nonlinear dynamics in arbitrary fibers," *Appl. Opt.* **44**(20), 4408–4411 (2005).
28. J. Liao, M. Marko, X. Li, H. Jia, J. Liu, Y. Tan, J. Yang, Y. Zhang, W. Tang, M. Yu, G. Q. Lo, D. L. Kwong, and C. W. Wong, "Cross-correlation frequency-resolved optical gating and dynamics of temporal solitons in silicon nanowire waveguides," *Opt. Lett.* **38**(21), 4401–4404 (2013).
29. C. A. Husko, P. Colman, S. Combrié, A. De Rossi, and C. W. Wong, "Effect of multiphoton absorption and free carriers in slow-light photonic crystal waveguides," *Opt. Lett.* **36**(12), 2239–2241 (2011).
30. A. Baron, A. Rysanyanskiy, N. Dubreuil, P. Delaye, Q. Vy Tran, S. Combrié, A. de Rossi, R. Frey, and G. Roosen, "Light localization induced enhancement of third order nonlinearities in a GaAs photonic crystal waveguide," *Opt. Express* **17**(2), 552–557 (2009).

---

## 1. Introduction

With the capability to tightly confine optical modes [1,2], the extremely large nonlinear effects enhanced by slow-light effects [3–7], and the compatibility with mature CMOS technologies [8], the Silicon photonic crystal waveguides (Si PhCWs) have been attracting increasing attention in recent years [1–9]. A variety of photonic technologies such as temporal

soliton-effects compression [10] have been demonstrated in silicon PhCWs, as well as in silicon nanowires and GaInP PhCWs [11,12], also including four-wave-mixing [13–16], optical filter [17], optical switching [18], all-optical modulation [19], all-optical wavelength conversion and ultralow-power all-optical signal processing [20–23]. All the recent and further applications of Si PhCWs are determined by the inside pulses evolution, which is usually affected by group velocity dispersion (GVD) and various slow-light enhanced nonlinear effects including self-phase modulation (SPM), two-photon absorption (TPA), free carrier absorption (FCA) and free carrier dispersion (FCD) [24].

With advantage of unambiguous temporal direction and high sensitivity, the sum-frequency generation cross-correlation frequency-resolved optical gating (SFG-XFROG), which derives from second-harmonic generation frequency-resolved optical gating (SHG-FROG), has been widely performed in ultrashort pulses measurements [25–28]. We applied the SFG-XFROG technique to investigate the pulse evolution in the Si PhCWs, particularly the pulse acceleration and the ultra-low power pulse evolution. As the unknown pulses are scanned by the pre-characterized reference pulses instead of the unknown pulses themselves, the SFG-XFROG provides the ability to detect ultralow power ultrashort pulses with unambiguous temporal profile. However, the pre-characterized reference pulses should be measured precisely and unambiguously, especially the temporal pulse profile.

We perform a SHG-FROG/SFG-XFROG setup to investigate the soliton dynamics in the slow light silicon PhCWs. Combining with nonlinear Schrödinger equation (NLSE) numerical simulations and optical spectrum analyzer (OSA) measurements, temporal and spectral profiles of the reference pulses will be determined prior, which supports the SFG-XFROG for measuring the pulses from the silicon PhCWs precisely and unambiguously. Regardless of large loss induced by the TPA which prevents pulse compression in the silicon photonic nanowire waveguide (SPNW), the results demonstrated that pulse compression have been realized in the silicon PhCWs. The slow-light enhanced pulse acceleration and spectral blue shift are also observed experimentally at much lower pulse energy than that required for the SPNW, which help to reveal the pulses dynamics in the silicon PhCWs, i.e. the impact of the slow-light effects on the soliton compression, the pulse acceleration and the spectral blue-shift.

## 2. Experimental setup, basic properties of the silicon PhCWs and NLSE modeling

The experimental setup with functions of both second-harmonic generation frequency resolved optical gating (SHG-FROG) and sum-frequency generation cross-correlation frequency resolved optical gating (SFG-XFROG) is shown in Fig. 1, in which a high-resolution sensitive grating spectrometer (Horiba JY 1000M-II with back-illumination deep-depletion CCD detector) and a 1 mm thick BBO crystal are aligned to detect pulses with ultralow energy down to less than 1.0 fJ. The setup can measure either the SHG-FROG data or the SFG-XFROG data of the pulses, which chosen function is controlled by the flip beam splitter.

The picosecond pulses, which with near-transform-limited 2.3 ps pulse-width and 39.1MHz repetition rate, are generated by a PolarOnyx Saturn mode-locked fiber laser with tunable wavelength range from 1533.5 nm to 1568 nm. The beams into and output from the waveguide are coupled in free space so as to minimize nonlinear fiber effects. A linear polarizer and a half wave-plate are utilized to ensure that the pulses coupled into the waveguide are in transverse-electric polarization. The output spectra from the waveguide are retrieved based on the XFROG measured data, and simultaneously measured by the OSA.

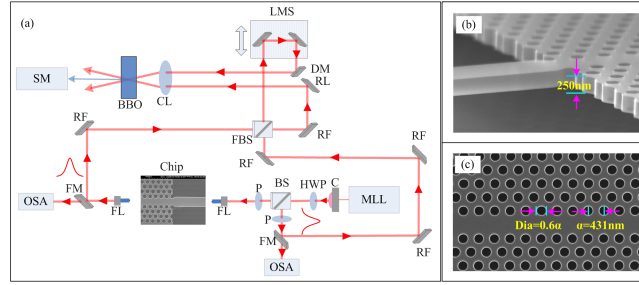


Fig. 1. (a) Experimental setup with combination of SFG-FROG and SFG-XFROG. MLL, mode-locked fiber laser; HWP, half waveplate; C, optical collimator; BS, beam splitter; P, polarizer; FL, focus lens; FM, flip mirror; OSA, optical spectrum analyzer; RF, reflector; FBS, flip beam splitter; DM, D-shape mirror; LMS, linear motorized stage; CL, bi-convex lens; BBO, barium borate crystal plate; SM, Spectrometer with CCD. The Scanning electron micrograph of the PhCWs in the angle of view at 45 degree (b) and 0 degree (c), with the marked main parameters of the PhCWs, including the waveguide thickness, the lattice constant and the hole diameter.

The employed hexagonal photonic crystal waveguides chip is fabricated by optimized deep-ultraviolet lithography on a silicon-on-insulator wafer with 250 nm device thickness and a 3  $\mu\text{m}$  buried oxide thickness, in which the undercladding sacrificial oxide is selectively etched to form a suspended silicon nanomembrane with top and bottom air cladding, as shown in Fig. 1(b). The lattice constant ( $\alpha$ ) and the hole diameter of the photonic crystal are 431 nm and  $0.60\alpha$  ( $\sim 260$  nm) respectively, with a single row line-defect to form a slow light photonic crystal waveguide with  $3550\alpha$  ( $\sim 1.5\text{mm}$ ) length, and the total length of the two access Si nanowires on both ends is about 2.0mm. The group indices  $n_g$  and the dispersion properties of the PhCWs measured by the coherent swept wavelength interferometry are illustrated in Fig. 2. The group index is about 10 at 1550nm wavelength and will increase with the longer wavelength, which will enhance the nonlinear effects and make the input pulse interact sufficiently with the waveguide so as to induce large nonlinear changes in a short optical length. With the slow light enhancement, the group velocity dispersion (GVD) and the third order dispersion are about  $1000\text{ ps}^3/\text{m}$  at 1550nm and  $-2000\text{ ps}^2/\text{m}$  at 1555nm wavelength respectively, which are about  $10^3$  times of which for the Si nanowires [28] so that the access Si nanowires can be neglected for the analysis.

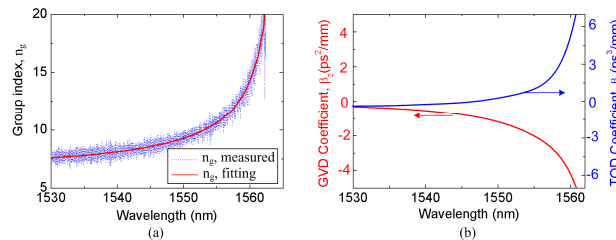


Fig. 2. (a) The group indices  $n_g$  of the utilized waveguide, with blue dot line and red solid line denoting the measured and the fitting  $n_g$  respectively. (b) GVD coefficient  $\beta_2$  and TOD coefficient  $\beta_3$  of the utilized waveguide. The red and blue solid line denotes  $\beta_2$  and  $\beta_3$  respectively.

The evolution of picosecond pulses in the PhCWs can be governed by the NLSE model with auxiliary carrier dynamics as below [5,12]:

$$\frac{\partial A}{\partial z} + \frac{i\beta_2}{2} \frac{\partial^2 A}{\partial t^2} - \frac{\alpha_{eff}}{2} A = i(\gamma_{eff} - \alpha_{TPA,eff}) |A|^2 A + (ik_0 k_{c,eff} - \frac{\sigma_{eff}}{2}) N_c A \quad (1)$$

$$\frac{\partial N_c(z,t)}{\partial t} = \frac{\alpha_{TPA,eff}}{2h\nu_0} |A(z,t)|^4 - \frac{N_c(z,t)}{\tau_c} \quad (2)$$

For the two considered wavelengths, i.e. 1550nm and 1555nm, the GVD parameter  $\beta_2$  are  $-900\text{ps}^2/\text{m}$  and  $-1800\text{ps}^2/\text{m}$ ; the effective linear loss coefficients are  $2\text{dB}/\text{mm}$  and  $2.6\text{dB}/\text{mm}$ ; the effective Kerr coefficients are  $9.46 \times 10^2 (1/W \cdot m)$  and  $1.02 \times 10^3 (1/W \cdot m)$ ; the effective TPA coefficients are  $8 \times 10^{-12} (m/W)$  and  $13.4 \times 10^{-12} (m/W)$ ; the effective parameters  $k_{c,eff}$  and  $\sigma_{eff}$  of the free carrier are  $-11.8 \times 10^{-27} m^3$ ,  $-13.3 \times 10^{-27} m^3$  for 1550nm, and  $3.57 \times 10^{-21} m^2$ ,  $4.62 \times 10^{-21} m^2$  for 1555nm respectively. The free carrier lifetime is estimated to be 0.5ns.

### 3. Pre-characterization of the reference pulses for SFG-XFROG measurements

As the scanning pulses, the references pulses should be precisely and unambiguously pre-characterized for the SFG-XFROG measurements. The reference pulses are measured prior by the SHG-FROG experimental setup. However, both temporal forms of the reference pulses retrieved from the SHG-FROG are reasonable, as shown in Fig. 3(a), which are reversal of each other. When the SFG-XFROG is tuned to work for high sensitivity, the reversal reference pulses will lead to much different retrieved results.

Associated with the OSA measurements, the SFG-XFROG measurements and the retrieved results of the output pulses from the PhCWs, the temporal and spectral profiles of the reference pulses can be determined precisely and unambiguously from the SHG-FROG measurement data.

The input pulses of 1550 nm and 1555 nm wavelength are employed for the measurements. The temporal and spectral properties of the reference pulses provided by the SHG-FROG measurements and the OSA measurements are shown in Fig. 3, in which the curves in Fig. 3(a) and 3(b), 3(c) and 3(d) are retrieved from the same SHG-FROG measurement data for 1550 nm and 1555 nm wavelength respectively. Obviously, the retrieved temporal pulse profile may be reversal of each other, i.e. the minor peaks may locate in the pulse tailing (tailing case) or head (head case). Furthermore, the phase and the spectral distributions are different between the two cases, in which only one case is true.

According to Fig. 3(b) and 3(d), the retrieved spectral curves of the tailing case, rather than the head case, are highly similar to the OSA measurement spectral curves, which indicates that the tailing case should be the only true one and will be further confirmed in the PhCWs measurements. Therefore, the difference between the retrieved spectra and the OSA measurement spectra can provide a valuable basis for the reference pulses temporal profile determination for the SHG-FROG measurements.

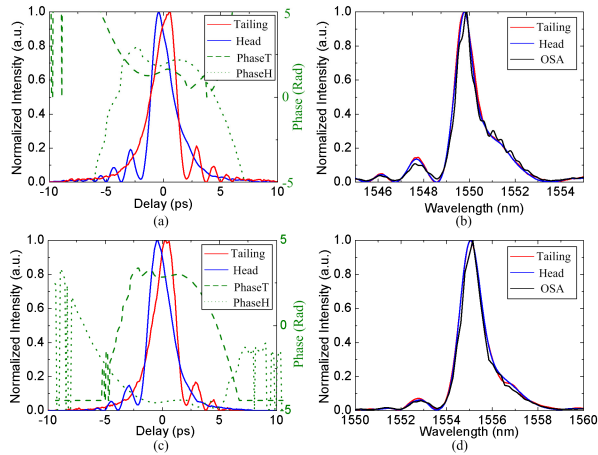


Fig. 3. The temporal and spectral properties of the reference pulses provided by SHG-FROG and OSA measurements. (a), (b) 1550 nm; (c),(d) 1555nm. In sub-figure (a) and (c), the red and the blue solid line denote the retrieved temporal intensity distributions with minor peaks locating in the pulse tailing and head respectively, and the corresponding phase distributions are denoted by green dashed line and green dotted line. In sub-figure (b) and (d), the red and blue solid line denote the retrieved spectra respectively, with the OSA measured spectra denoted by the dark solid line.

The input pulses for the PhCWs have the same profiles as the reference pulses. The input pulse energy ranges from several fJ to more than 20pJ. The SFG-XFROG retrieved spectra are shown in Fig. 4, in which the NLSE simulation spectra and the OSA measurement spectra of the output pulses from the PhCWs with input pulse energies of 8.6pJ and 12.9pJ are shown for 1550 and 1555 nm wavelength respectively. For the two cases of reference pulses profiles, the SFG-XFROG retrieved spectra and the NLSE simulated spectra have two corresponding possibilities. Obviously, owing to sufficient nonlinear properties induced by the large nonlinearity of the PhCWs, the temporal profile of the reference pulse will determine the SFG-XFROG retrieved and the NLSE simulated output pulses significantly.

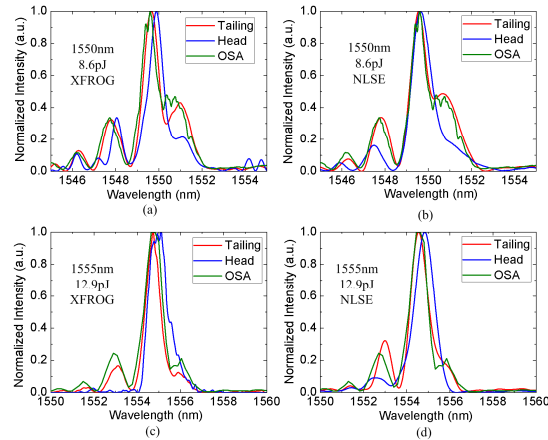


Fig. 4. The spectra of the output pulses from the PhCWs for SFG-XFROG retrieves, NLSE simulations, and OSA measurements. (a), (b) 1550 nm; (c),(d) 1555nm. The inset 8.6pJ and 12.9pJ denote the input pulse energies. For all sub-figures, the red and blue solid lines denote the spectra of the retrieved output pulses for the tailing case and the head case respectively, and green solid lines denote the spectra measured by the OSA.

According to Fig. 4, the difference between the SFG-XFROG retrieved spectra and the OSA measured spectra, and that between the NLSE simulated spectra and the OSA measured spectra, are remarkable for both input pulses profile cases. The discrepancy parameter (DP) is defined in Eq. (3) to estimate the difference for the reference pulses temporal profile determination process,

$$DP = \frac{\int [I_{\alpha}(\lambda) - I_{OSA}(\lambda)]^2 d\lambda}{\int I_{OSA}^2(\lambda) d\lambda} \quad (3)$$

Where  $I_{\alpha}(\lambda)$  is the SFG-XFROG retrieved or the NSLE simulated spectral intensity of the output pulse from the PhCWs, and  $I_{OSA}(\lambda)$  is the OSA measured spectral intensity. When the DP value is small, it indicates that the spectra are similar to the OSA measured data which can be considered to be precise for spectral measurement. The DP plots for various input pulse energies and center wavelengths are shown in Fig. 5.

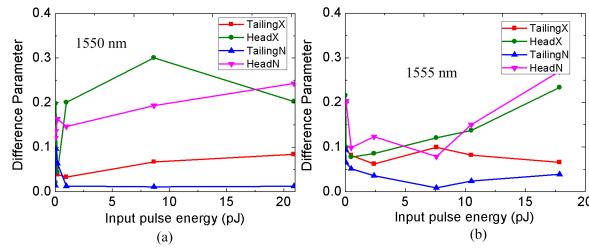


Fig. 5. The discrepancy parameter (DP) plots of the spectra retrieved from the SFG-XFROG measurements and the NLSE simulations at central wavelength 1550nm (a) and 1555 nm (b). The red line with squares and the green line with circles denote the DF of the SFG-XFROG retrieved spectra for tailing case and head case respectively. The blue line with upward triangles and the magenta line with downward triangles denote the DF of the NLSE simulation spectra for tailing case and head case respectively.

For the two input center wavelengths, i.e. 1550 nm and 1555 nm, the DP values keep smaller than 0.1 for various input pulse energies for the tailing case, while the DP values are larger than 0.3 for the head case. At the same time, the DP values of the NLSE simulated spectra are small and with the same trend as those of the SFG-XFROG retrieved spectra.

Therefore, all the above comparisons between the OSA measured spectra and the SHG-FROG/SFG-XFROG retrieved or the NLSE simulated spectra suggest that, the tailing case is the true temporal reference pulses, which suggests that it is valid to determine unambiguously the temporal profile of the reference pulses by this method. In the following analysis, the reference pulses with tailing case temporal profile will be utilized.

#### 4. Evolution of the soliton in the PhCWs

With the pre-characterized reference pulses for the experimental setup as shown in Fig. 1, the picosecond soliton evolution in the PhCWs is analyzed experimentally and numerically.

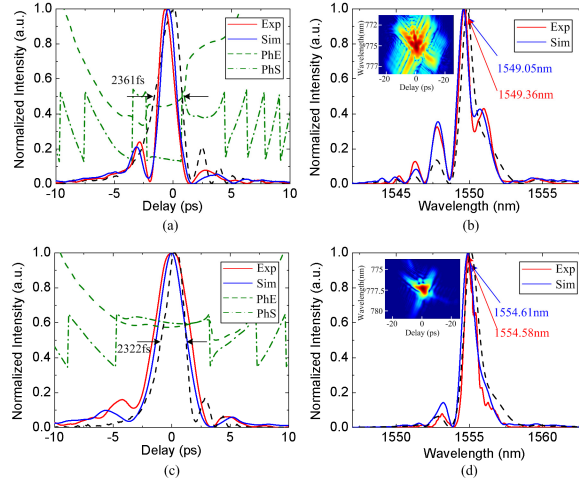


Fig. 6. Temporal intensity with phase distribution and spectra profile of the output pulses at 8.6pJ and 4.1pJ input pulse energies for 1550nm and 1555nm respectively. (a) and (b)1550 nm; (c) and (d)1555nm. Red curves, experimental results; blue curves, simulation results; black dashed curve, input profiles; green dotted line, phase distribution from SFG-XFROG retrieved; green dashed dot line, phase distribution from NLSE simulation. The temporal duration of the input pulses are marked in (a) and (c). Insets in (b) and (d) are the SFG-XFROG retrieved traces.

Figure 6 shows the SFG-XFROG measured and the NLSE simulated output pulse for the input pulse energy of 8.6pJ at 1550nm and 4.1pJ at 1555nm center wavelength respectively, in which the initial pulses for the NLSE simulations are the same as those for the experimental measurements. The parameters for the NLSE simulations are illustrated in Fig. 2, in which the group velocity indices are 8.5 and 11, and the GVD coefficients are  $-900\text{ps}^2/\text{m}$  and  $-1800\text{ps}^2/\text{m}$ , while the TOD coefficients are  $0.2\text{ps}^3/\text{mm}$  and  $0.6\text{ps}^3/\text{mm}$  for 1550nm and 1555nm center wavelength respectively. The slow light effects are also taken into account by scaling factor  $n_g/n_0$  [29,30], where  $n_g$  is the group velocity index and  $n_0$  is the refractive index of the silicon.

The NLSE simulated results show remarkable agreements with the SFG-XFROG retrieved results in the temporal and spectral intensity distributions with phase distributions. Remarkably, the pulses compression ratio at 1550nm center wavelength is  $R_{com} = 1.53$  ( $R_{com} = T_{in} / T_{com} = 2361\text{fs} / 1539\text{fs}$ ), while the pulses are broaden at 1555nm center wavelength with broadening ration  $R_{bro} = 1.44$  ( $R_{bro} = T_{bro} / T_{in} = 3353\text{fs} / 2322\text{fs}$ ). Basically, lower input pulse energy and higher group velocity dispersion for 1555nm center wavelength makes the group velocity dispersion play a key role in the pulse evolution, so that the output pulses exhibit broadening instead of compression. The nearly flat form of the temporal phase distributions further support the high-order soliton compression at 1550nm and the fundamental soliton holding at 1555nm center wavelength. At the same time, the spectral blue shift induced by the FCD [28] is about 0.5 nm and 0.2 nm for 1550nm and 1555nm center wavelength respectively.

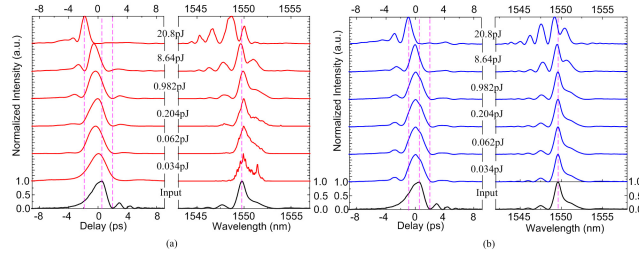


Fig. 7. Temporal and spectral intensity profiles of the output pulses for increasing coupled pulse energies from 68 fJ to 25.6 pJ. (a) Retrieved results from SFG-XFROG measurements; (b) Numerically predicted results from NLSE simulations. Input pulse profiles are also shown in black at the figure bottom. The central labels denote the input pulse energies.

For the input pulses with 1550nm center wavelength, the output pulse profiles for various input pulse energies are shown in Fig. 7(a) and 7(b), which indicate that the SFG-XFROG retrieved results agree with the NLSE simulated results remarkably. Obviously, high-order soliton compression will occur when the pulse energy is raised to a certain level, which will not occur in the SPNW [25,28] even if the pulse energy is at the same level due to the pulse energy being reduced by the nonlinear loss while transmitting. According to Fig. 7(a) and 7(b), when the input pulse duration is 2.36ps and the pulse energy is 20.8pJ, the pulse will be compressed to 1095fs (the compression ratio is 2.15), and the corresponding soliton order is  $N = 2.27$  ( $N = (L_D/L_{NL})^{1/2} = (T_0^2 \gamma_{eff} P_0 / |\beta_2|)^{1/2}$  [10,25,28], where  $T_0$  and  $P_0$  are the input pulse duration and the pulse energy,  $\gamma_{eff}$  and  $\beta_2$  are the enhanced nonlinear parameter and GVD coefficient respectively). While with the same input pulses, the pulses will be broadened by 1.67 times for the same length SPNW. The pulse acceleration will be more remarkable when the input pulse energy increases, and the maximal pulse acceleration will be 1982fs at input pulse energy of 20.8pJ, which is much lower than 98.2pJ which required for the SPNW to achieve pulse acceleration of 1328fs. Furthermore, the pulse spectra exhibits increasing broadening accompanied with splitting and blue shift, which should be induced by SPM and FCD respectively [30]. The spectra blue shift is about 1.43nm at the input pulse energy of 20.8pJ for the Si PhCWs, which is much lower than 98.2pJ which required to achieve 2.86nm blue shift for the SPNW [28].

Obviously, the slow light effects enhance the nonlinear process significantly, which leads to remarkable pulse compression, acceleration and spectral blue shift in a short waveguide even for low input pulse energy. The slow light effects are involved in the NLSE simulations with the slow light enhanced nonlinear parameter  $(n_g/n_0)^2 \gamma$  and the TPA coefficient  $(n_g/n_0)^2 \alpha_{TPA}$  [5]. The free carrier absorption parameter  $\sigma$  and the dispersion parameter  $k_c$  are enhance by  $n_g/n_0$  [5,29,30].

Figure 8 shows how the slow light effects affect the pulse dynamics. As illustrated in Fig. 8(a), the slow light enhances the pulse compression and the pulse acceleration, as well as the spectral blue shift. Figure 8(b) indicates that the pulse compression is remarkably enhanced by the slow light effects. Basically, the slow light effects make the nonlinear length  $L_{NL} = 1/\gamma P_0$  be shortened to  $L_{NL} = (n_0/n_g)^2 \cdot 1/\gamma P_0$ , which will result in a higher soliton order and then lead to a large pulse compression even at low pulse energy level. While at the same input pulse energy level, the pulse shows broadening for 1555nm, which results from the large GVD dispersion, as the corresponding GVD length ( $L_D = T_0^2 / |\beta_2| = 0.98\text{mm}$ ) is shorter than the waveguide length (1.5mm). The energy ratio of pulse center within the full width of half-max (FWHM) is denoted by data stars with suitable color in Fig. 8(b), which are in red

and blue color for 1550nm and 1555nm wavelength respectively. The energy ratios of pulse center for the output pulses at 1550nm center wavelength are larger than that at 1555nm center wavelength for the same input pulse energy level. However, the energy ratios of pulse center for maximal compression pulses are 0.48 and 0.63 for 1550nm and 1555nm wavelength respectively, which indicates that the pulse energy for the main peak will be reduced when being compressed.

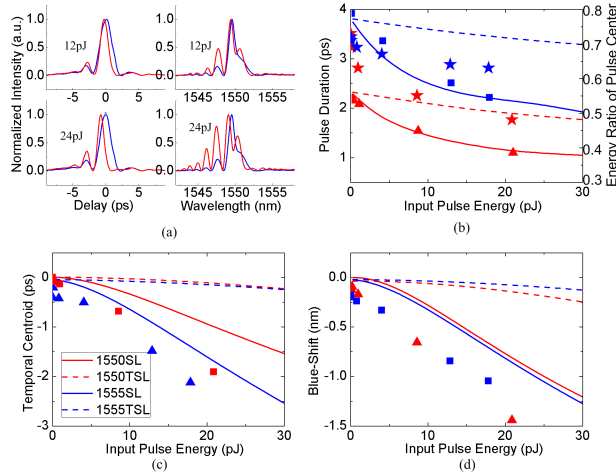


Fig. 8. The effects of slow light on the pulse dynamics by NLSE simulations and SFG-XFROG experiments. (a) The temporal and spectral intensity profiles for input pulse energy of 12pJ and 24pJ at 1550nm by NLSE simulation, the red curves denote considering slow light effects, while blue curves denote turning off the slow light effects. The pulse duration and the energy ratio of pulse center (b), the temporal pulse centroid (c) and the spectral blue shift (d) with respect to the increasing input pulse energy. The red solid lines and the blue solid lines denote the cases considering slow light enhancement for the central wavelength of 1550nm and 1555nm respectively, while the red dashed lines and the blue dashed line denote the cases turning off the slow light enhancement. The experimental measurements are denoted by blue data squares and red data triangles, and the energy ratios of the pulse center are denoted by red and blue stars for the 1550nm and 1555nm wavelength respectively.

As shown in Fig. 8(c), the pulse acceleration is significantly enhanced by the slow light effects, reaching to nearly 2ps and 3ps for the examined wavelengths. The FCA and FCD are enhanced by  $(n_g/n_0)^3$ , in which the FCA and FCD parameters  $\sigma$  and  $k_c$  are enhanced by  $n_g/n_0$ , while the TPA coefficient  $\alpha_{TPA}$  is enhanced by  $(n_g/n_0)^2$  [5]. The FCA just leads to an asymmetric absorption of the pulse, while the FCD leads to the refractive index decreasing and the spectral blue-shift remarkably, which results in significant pulse acceleration at seriously negative dispersion region of the PhCWs. Therefore, the FCD is mainly responsible for the pulse acceleration. As the group velocity indices of the Si PhCWs are 11 and 8.5 for 1555nm and 1550nm wavelength respectively, the pulse acceleration is more remarkable for the case of 1555nm.

It is shown in Fig. 8(d) that the spectral blue shift is enhanced by the slow light effects, which are more than 1nm for both examined wavelengths. The phase modulation by FCD has a sign opposite to that of the SPM, and both processes are related to the peak power, which compete with each other to result in a higher power for the certain spectral blue shift. The pulse broadening will reduce the pulse peak power, which is responsible for smaller blue shift at 1555nm center wavelength.

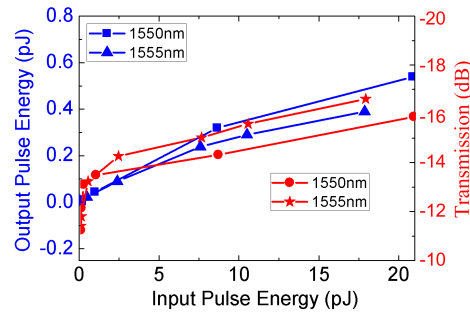


Fig. 9. The output pulse energy and transmission relative to increasing input pulse energy by experiment.

The output pulse energies and the transmissions for various input pulse energies are shown in Fig. 9. The output pulse energy will increase nonlinearly with the input pulse energy, while the transmission will decrease nonlinearly which is mainly dominated by nonlinear TPA. The output pulse energy is 0.54pJ and 0.39pJ for the two examined wavelengths with input pulse energy of 20.8pJ and 17.9pJ respectively, while the transmission is  $-15.8\text{dB}$  and  $-16.6\text{dB}$ .

## 5. Conclusion

By the SHG-FROG/SFG-XFROG setup with unambiguous pre-characterized reference pulses and the NLSE modeling simulations, we have demonstrated the optical soliton evolution in the silicon PhCWs unambiguously to find out how the slow light effects affect the pulse evolution. Regardless of the inevitable nonlinear TPA in the Silicon which prevents the soliton compression to occur in the short SPNW, the retrieved temporal pulse profiles show that high-order soliton compression can be achieved in short Si PhCWs by compression ratio 2.27 at the input pulse energy of 20.8pJ, owing to the slow light enhanced GVD and nonlinearities. Furthermore, the pulses acceleration and the spectral blue shift which mainly induced by FCD have also been observed both by the SFG-XFROG measurements and the NLSE modeling simulations, which indicate that the pulses compression, the pulses acceleration and the spectral blue shift are significantly enhanced by the slow light effects.

Basically, FCA and FCD is enhanced by slow light effects by parameter  $(n_g/n_0)^3$ . Besides, the determination method for the temporal pulse profile of the reference pulses has been realized by combining the SHG-FROG/SFG-XFROG measurements, the NLSE simulations and the OSA measurements, which supports the precise and unambiguous measurements of the ultrashort laser pulses by the high sensitive SFG-XFROG.

## Acknowledgments

The authors acknowledge assistance from James F. McMillan, Jiangjun Zheng and Ken Liu during our experiments. This research was funded by the National Natural Science Foundation of China (NSFC) under Grant NO. 61070040, 61108089, 61205087 and 61107005, and by the NSF ECCS-1102257 and IGERT-1069240.